arXiv:2507.09038v2 [q-bio.CB] 29 Nov 2025

A PHASE-FIELD MODEL FOR APOPTOTIC CELL DEATH

DANIEL A. VAUGHAN[1,2], ANNA M. PICCININI[2], MISCHA ZELZER[2], ETIENNE FARCOT[1], BINDI S. BROOK[1], KRIS VAN-DER-ZEE[1], AND LUIS ESPATH[1]

Abstract. The process of programmed cell death, namely apoptosis, is a natural mechanism that regulates healthy tissue, multicellular structures, and homeostasis. An improved understanding of apoptosis can significantly enhance our knowledge of biological processes and systems. For instance, pathogens can manipulate the apoptotic process to either evade immune detection or to facilitate their spread. Furthermore, of particular clinical interest is the ability of cancer cells to evade apoptosis, hence allowing them to survive and proliferate uncontrollably. Thus, in this work, we propose a phase-field framework for simulating intrinsic or extrinsic apoptosis induced by an activation field, including deriving the configurational mechanics underlying such phenomena. Along with exploring varying conditions needed to initiate or reduce apoptosis, this can serve as a starting point for computational therapeutic testing. To showcase model capabilities, we present simulations exhibiting different types of cellular dynamics produced when varying the mechanisms underlying apoptosis. The model is subsequently applied to probe different morphological transitions, such as cell shrinkage, membrane blebbing, cavity formation and fragmentation. Lastly, we compare the characteristics observed in our simulations to electron microscopy images, providing additional support for the model.

AMS subject classifications: · 74N20 · 92B05 · 74F25 · 92C15

Contents

1. Introduction 2
2. A continuum theory for apoptotic processes 4
2.1. Variational chemo-mechanical formulation 4
2.2. Thermodynamic potential 5
2.3. Specialisation to directional apoptosis 5
2.4. Dimensionless Form 6
3. Numerical Simulations 6
3.1. Physical and Numeric Parameter list 6
3.2. Initial conditions 7
3.3. Finger formation and nucleation during apoptosis 7
3.4. Interface width influence 7
3.5. Varying the rate of reaction and annihilation 9
3.6. Internal configurational forces 10
4. Qualitative comparison of electron microscopy images and simulations 14
5. Conclusions 18
6. Acknowledgments 18
7. Data Availability 18
Appendix A. Configurational mechanics 18
References 20

1. School of Mathematical Sciences, University of Nottingham, Nottingham, United Kingdom, NG7 2RD, 2. School of Pharmacy, University of Nottingham, Nottingham, United Kingdom, NG7 2RD

E-mail address: luis.espath@nottingham.ac.uk.

Date: December 2, 2025.

1. Introduction

Apoptosis, the process of programmed cell death, is a key component in a range of processes including cellular turnover, robust immune response to pathogens, embryonic development and chemical-induced cell death [10]. Irregularities in this process, resulting in either enhanced or reduced apoptosis, are a causative factor in many human diseases, such as autoimmune and neurodegenerative disorders (excessive cell loss precipitating conditions such as Alzheimer's disease) and many types of cancer (inadequate cell clearance) [3, 5, 25]. Hence, the ability to modulate and understand the life or death of a cell is of high interest. Apoptotic cells can be identified by their distinct morphological features. These include separation from other cells, chromatin condensation and DNA fragmentation, irregular bulging in the plasma membrane (finger formation), cell shrinkage, and the formation of apoptotic bodies, which are then degraded in lysosomes [23, 1]. These morphological changes can be observed using microscopy techniques, with electron microscopy providing superior cellular details and reproducibility compared to light microscopy [17]. The highly complex and sophisticated mechanisms of apoptosis can be triggered by a range of factors, including components of the immune system and cytotoxic molecules administered as part of a chemotherapeutic regimen [10]. Given the complexity of apoptosis, a thorough understanding of how environmental cues shape this process could provide a valuable platform for devising targeted therapies and refining diagnostic strategies.

Apoptosis can be initiated by one of two canonical pathways, see for instance, Lossi [20].

(i) Intrinsic (mitochondrial) pathway: triggered by intracellular stresses such as DNA damage, oxidative imbalance, growth-factor withdrawal, or protein misfolding. These cues promote mitochondrial release of cytochrome c, which activates a cascade of proteases (caspases) that orchestrate cellular disassembly.

(ii) Extrinsic (death-receptor) pathway: initiated by extracellular ligands binding to surface receptors such as Fas or TNF, which in turn activate the same downstream caspase machinery.

In this work, we refer to these mechanisms as intrinsic and extrinsic apoptosis, respectively. Irrespective of the initiating route, apoptosis involves a spatially distributed biochemical activation field that drives the progressive breakdown of cytoskeletal and organelle structures. Mathematically, this activation field is modelled in an agnostic manner, without distinguishing whether its origin is intrinsic or extrinsic. This activation field regulating death is referred to as the apoptotic phase, while the field representing the cell itself is denoted the cyto phase.

Moreover, according to Mustafa et al. [22], the extrinsic pathway begins when death ligands, such as TNF-α or Fas ligand, bind to their specific receptors on the cell membrane. In contrast, the intrinsic pathway involves permeabilisation of the outer mitochondrial membrane and the subsequent release of apoptogenic factors, including cytochrome c, under the control of Bcl-2 family proteins. Both routes lead to a cascade of biochemical reactions that activate caspases, fragment DNA, and promote the systematic disassembly of cellular structures.

In this study, we develop a multi-component phase-field model incorporating biochemical reactions between a cyto phase (cell) and an apoptotic phase (triggered by the intrinsic or extrinsic apoptosis mechanism), to understand and model the physical characteristics exhibited by a cell undergoing apoptosis. This employs a coupled set of partial differential equations for the phase fields φ (cyto phase) and σ (apoptotic phase). Phase-field modelling of apoptosis remains a relatively unexplored area of modelling for cellular dynamics and therefore provides an opportunity for this model to serve as a novel tool for investigating apoptosis. The use of multi-component phase-field models with reaction equations is well-established, with extensive literature not only in general contexts [2, 14, 21], but also in applications to biological phenomena, with published work to date focusing predominantly on modelling cell growth [26, 16, 9]. To obtain a chemo-mechanical phase-field model to produce the desired dynamics of finger formation, we take inspiration from Kobayashi's work on solidification [18]. Furthermore, to ensure the reaction component of the apoptosis model stays within certain bounds, we utilise the same substitution as Kobayashi [18]. The apoptosis model is also inspired by the system proposed by Fried & Gurtin [13].

We address the need for a multi-component phase-field model for simulating apoptotic behaviour by developing a novel framework. The framework builds upon the mathematical structure for modelling reaction kinetics developed by Krambeck et al. [19], which examines the fundamental properties of constitutive laws in chemically reacting systems, focusing on common physical assumptions and mass-action-based rate expressions. It also calls on the mechanics of phase-field models proposed by Clavijo et al. [8]. Additionally,

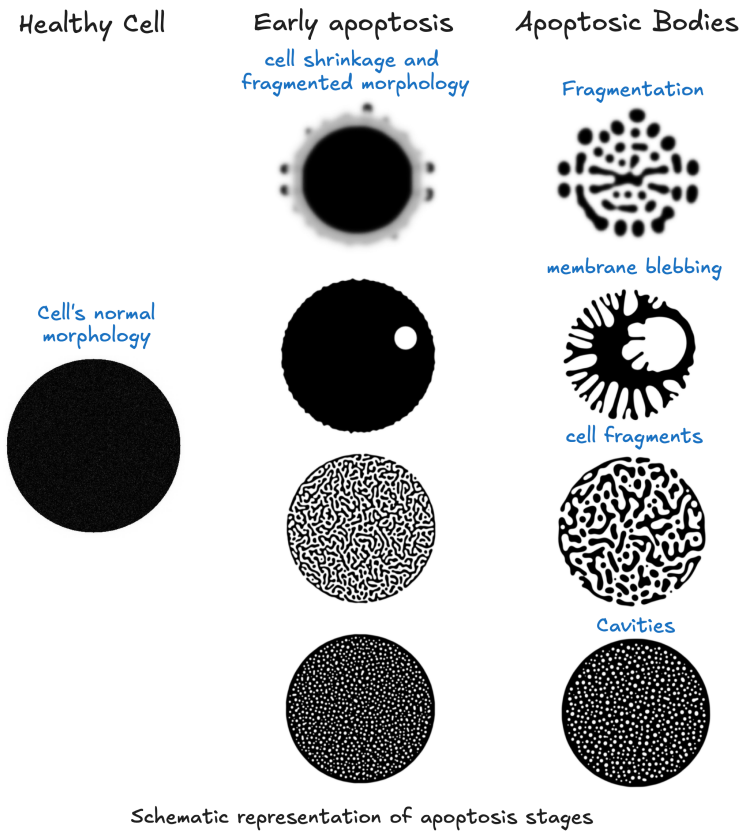

FIGURE 1. Schematic representation of apoptosis stages. The diagram illustrates the morphological progression from a healthy cell to apoptotic bodies. The stages include (left) normal morphology, (middle) early apoptosis characterised by cell shrinkage and membrane blebbing, and (right) advanced apoptosis showing fragmentation and formation of apoptotic bodies.

further work by Clavijo et al. [7] is also used, as it presents a unified, thermodynamically consistent framework for modelling multicomponent, solid systems undergoing coupled diffusion and chemical reactions. In their work, Clavijo et al. developed the extended Larché–Cahn framework to simulate how chemo-mechanical and reactive processes drive phase separation, domain evolution, and microstructural changes.

Numerical simulations illustrating finger formation (membrane blebs), nucleation and fragmentation are implemented in the Dedalus package [4]. This package allows for rapid mathematical development through the symbolic implementation of the system into the numerical solver. Furthermore, it allows for temporal and spatial analysis in 1, 2, and 3-dimensional domains with minimal alterations to pre-existing code for higher-dimensional simulations.

To demonstrate the model's capabilities, we provide a comparison of numerical simulations at selected time points and their similarity with real-world experimental data (electron microscopy images from You et al. [27]) in two morphological categories: membrane blebbing (or finger formation) and size and number of cavity formations (throughout cavity formations will be referred to as nucleations). In this manuscript, we describe nucleations as a void (φ=0) surrounded by the phase field $\varphi = 1$ and fragments as an area occupied by $\varphi = 1$ and surrounded by a void (φ=0). While variability of biological systems does result in significant differences between images, we demonstrate that there are consistent similarities between the model output and cell imaging.

In Section §2, we develop a chemo-mechanical phase-field model to describe the dynamics of the cyto phase φ and the apoptotic phase fields σ, including the system that produces features observed in biological cells undergoing apoptosis. In Section §3, we present computational simulations, used to illustrate finger

formation, nucleation, and cell fragmentation during the degradation of the cyto phase field φ. Furthermore, in Section §4, we compare finger formation, nucleation, and cell fragmentation with electron microscopy images from You et al. [27]. As mentioned, continuum models for apoptosis remain largely unexplored, presenting a unique opportunity not only to extend the utility of these models to a new biological context, but also to gain mechanistic insight into the interplay between chemical signalling and mechanical deformation during programmed cell death. In Section In Appendix §A, we present the mathematical derivation of the underlying configurational mechanics, including configurational forces and the configurational balance law.

2. A continuum theory for apoptotic processes

Although the precise molecular genesis of apoptosis remains an open question in biology, our model purposefully abstracts this uncertainty by focusing on the downstream enzymatic disassembly phase. The coordinated degradation of cytoskeletal and organelle structures while remaining agnostic to whether the apoptotic activation originates from intrinsic or extrinsic pathways.

To this end, consider the existence of two kinematic processes given by the phase fields φ and σ. The process φ shrinks and fades due to the presence of the process σ; therefore, we refer to φ as the cyto phase field and σ as the apoptotic phase field, triggering the enzymatic disassembly. To mimic the interplay between the cyto and apoptotic phases resulting in apoptosis, we adopted the framework from Clavijo et al. [6] to model reaction-driven annihilation, where the phase fields φ and σ are treated as the concentrations of two species[1], denoted by $\mathcal{A}_\varphi$ and $\mathcal{A}_\sigma$, with $\varphi := [\mathcal{A}_\varphi]$ and $\sigma := [\mathcal{A}_\sigma]$, the reaction describing these interactions is

$$\varsigma^r_\varphi \mathcal{A}_\varphi + \varsigma^r_\sigma \mathcal{A}_\sigma \xrightarrow{k} \varsigma^p_\varphi \mathcal{A}_\varphi, \tag{1}$$

where ς^r_φ, ς^r_σ, and ς^p_φ are the stoichiometric coefficients for the reactants and products, respectively, and k is the reaction rate constant.

2.1. Variational chemo-mechanical formulation.

Here, we introduce a degenerate irreversible reaction model that describes a chemical-initiated enzymatic disassembly of the cyto phase field initiated by the apoptotic phase field. This degenerate irreversible reaction is given by

$$r := \hat{k} g(\varphi)\, \sigma^{\varsigma^r_\sigma}, \quad \text{with} \quad g(\varphi) = \varphi(1-\varphi), \tag{2}$$

where $g(\varphi)$ promotes the development of the reaction at the interface; hence the degeneracy. Thus, the resulting internal mass supply rates for phase fields φ and σ are then

$$(\varsigma^p_\varphi - \varsigma^r_\varphi) r \qquad \text{and} \qquad -\varsigma^r_\sigma r, \tag{3}$$

where $(\varsigma^p_\varphi - \varsigma^r_\varphi) r$ represents the net production or depletion rate of the (cyto) phase field φ, while $-\varsigma^r_\sigma r$ corresponds to the vanishing rate of the apoptotic phase field σ at the expense of the enzymatic disassembly of the cyto phase field φ. Depending on the values of the stoichiometric coefficients, the evolution of the phase field φ can lead to either an increase or a decrease in the (cyto) phase field φ. For example, if $\varsigma^p_\varphi > \varsigma^r_\varphi$, then the phase field φ increases, signifying growth, while $\varsigma^p_\varphi < \varsigma^r_\varphi$ leads to a net depletion of the phase field φ. We propose the following coupled gradient flows to model the kinematic interplay between these processes, mimicking chemically induced apoptotic dynamics.

Next, we consider the following energy functional

$$\Psi[\varphi, \sigma] := \int_\Omega \psi(\varphi, \nabla\sigma, \nabla\varphi)\, \mathrm{d}v, \tag{4}$$

where the free-energy density ψ is given as a function of the two kinematic processes and their derivatives, namely

$$\psi(\varphi, \nabla\sigma, \nabla\varphi) = f(\varphi) + \begin{bmatrix} \nabla\varphi & \nabla\sigma \end{bmatrix} \cdot \mathbf{\Sigma} \begin{bmatrix} \nabla\varphi \\ \nabla\sigma \end{bmatrix}, \tag{5}$$

where f is a potential function depending on the phase field φ, and $\mathbf{\Sigma}$ is a symmetric positive definite matrix. The functional above splits the free energy into a potential function f, which may not be convex, and a regularisation term depending upon the gradients of the phase fields φ and σ.

[1] Although we treat the phase fields as concentrations when dealing with chemical reactions, these are mere representations of the underlying cyto and apoptotic agents.

Then, we associate the evolution of the phase fields and the chemical reactions with the gradient flow given by the energy functional (4) such that

$$\begin{bmatrix} \tau & 0 \\ -\beta & \alpha \end{bmatrix} \begin{bmatrix} \dot{\varphi} \\ \dot{\sigma} \end{bmatrix} - \begin{bmatrix} (\varsigma_\varphi^p - \varsigma_\varphi^r) r \\ -\varsigma_\sigma^r r \end{bmatrix} = \begin{bmatrix} -\dfrac{\delta \Psi}{\delta \varphi} \\ -\dfrac{\delta \Psi}{\delta \sigma} \end{bmatrix} \tag{6}$$

this can be written as,

$$\tau \dot{\varphi} - (\varsigma_\varphi^p - \varsigma_\varphi^r) r = -\frac{\delta \Psi}{\delta \varphi} \quad \text{and} \quad \alpha \dot{\sigma} - \beta \dot{\varphi} + \varsigma_\sigma^r r = -\frac{\delta \Psi}{\delta \sigma}, \tag{7}$$

where $\dot{\varphi} = \frac{\partial \varphi}{\partial t}$ and $\dot{\sigma} = \frac{\partial \sigma}{\partial t}$. Expression (7) describes the evolution of the phase fields φ and σ. The parameters that dictate the relaxation towards equilibrium are $\tau > 0$ for the phase field φ, and $\alpha > 0$ and $\beta > 0$ for σ. The first variation of $\delta\Psi$ with respect to the phase fields φ and σ are, respectively, given by

$$\frac{\delta \Psi}{\delta \varphi} = \frac{\partial \psi}{\partial \varphi} - \operatorname{div} \frac{\partial \psi}{\partial \nabla \varphi}, \qquad \text{and} \qquad \frac{\delta \Psi}{\delta \sigma} = \frac{\partial \psi}{\partial \sigma} - \operatorname{div} \frac{\partial \psi}{\partial \nabla \sigma}, \tag{8}$$

leading us to the following system

$$\begin{cases} \tau \dot{\varphi} - (\varsigma_\varphi^p - \varsigma_\varphi^r) r = -\left(\dfrac{\partial \psi}{\partial \varphi} - \operatorname{div} \dfrac{\partial \psi}{\partial \nabla \varphi} \right), \\ \alpha \dot{\sigma} - \beta \dot{\varphi} + \varsigma_\sigma^r r = -\left(\dfrac{\partial \psi}{\partial \sigma} - \operatorname{div} \dfrac{\partial \psi}{\partial \nabla \sigma} \right), \end{cases} \tag{9}$$

for which the phase fields φ and σ are periodic in Ω.

2.2. **Thermodynamic potential.** The thermodynamic potential, $f(\varphi)$, reflects a bistable state, promoting nontrivial equilibrium states for the phase field φ. We define it as

$$f(\varphi) = \frac{1}{4}\varphi^4 - \frac{1}{2}\varphi^3 + \frac{1}{4}\varphi^2. \tag{10}$$

The polynomial structure is chosen to create a double-well potential. This setup drives phase separation, shaping an energy landscape that enables transitions between metastable states.

2.3. **Specialisation to directional apoptosis.** To formulate a directional form of the system (9) for simulations, we consider the anisotropic evolution in the phase field φ. We introduce the anisotropy into Equations (9) through the free energy ψ in the term for $\mathbf{\Sigma}$, therefore we make $\mathbf{\Sigma}$ the following

$$\mathbf{\Sigma} = \begin{bmatrix} \dfrac{\epsilon^2}{2} & 0 \\ 0 & \dfrac{\gamma^2}{2} \end{bmatrix} \tag{11}$$

Let ϵ be a function of the gradient of the phase field φ. Thus, yielding the following system to describe directional anisotropy

$$\begin{cases} \tau \dot{\varphi} = -\left(\dfrac{\partial f}{\partial \varphi} - \operatorname{div} \left(\epsilon^2 \nabla \varphi - \epsilon \dfrac{\partial \epsilon}{\partial \theta} \nabla \times (\varphi \boldsymbol{e}_z) \right) \right) + (\varsigma_\varphi^p - \varsigma_\varphi^r) r, \\ \alpha \dot{\sigma} = \operatorname{div} \left(\gamma^2 \nabla \sigma \right) + \beta \dot{\varphi} - \varsigma_\sigma^r r, \\ \epsilon = \tilde{\epsilon}(\vartheta + \cos(\theta)), \\ \dfrac{\partial \epsilon}{\partial \theta} = -\tilde{\epsilon} \vartheta \sin(\theta), \\ \theta = \arctan \left(\dfrac{\partial_y \varphi}{\partial_x \varphi} \right), \\ r = g(\varphi) \hat{k} \sigma^{\varsigma_\sigma^r}, \end{cases} \tag{12}$$

where $\partial_{v_i}\varphi = \frac{\partial\varphi}{\partial v_i}$ denotes partial derivatives along coordinates v_i. This system models directional growth dynamics through an anisotropic diffusion term influenced by the gradient of the phase field φ, with $\epsilon(\theta)$ introducing spatial dependencies. To maintain numerical stability during simulations, we make an approximation for $r = g(\varphi)\hat{k}\sigma^{\varsigma_\sigma^r}$ of the following form

$$r = g(\varphi)\frac{k_1}{\pi}\arctan(k_2\sigma) \tag{13}$$

2.4. **Dimensionless Form.** To understand the key characteristics in the simulation that affect the nature of apoptotic death, we introduce a dimensionless form of the equations shown in Equation (9). Using the following dimensionless variables and parameters, $t = T\bar{t}$, $l = L\bar{l}$, and $rT = \bar{r}$ yields the following equations,

$$\dot{\varphi} = -\ell_f\frac{\partial f}{\partial\varphi} + \ell_\varphi \mathrm{div}\left[(\vartheta+\cos(\theta))^2\nabla\varphi + (\vartheta+\cos(\theta))\sin(\theta)\nabla\times(\varphi\boldsymbol{e}_z)\right] + \ell_r^\varphi\bar{r}, \tag{14}$$

and

$$\dot{\sigma} = \ell_1\Delta\sigma + \ell_2\dot{\varphi} - \ell_r^\sigma\bar{r}, \tag{15}$$

where where $\ell_f = T/\tau$, $\ell_\varphi = T\tilde{\epsilon}^2/L^2\tau$, $\ell_r^\varphi = (\varsigma_\varphi^p - \varsigma_\varphi^r)k_1/\tau$, $\ell_1 = \gamma^2 T/\alpha L^2$, $\ell_2 = \beta/\alpha$, and $\ell_r^\sigma = \varsigma_\sigma^r\bar{r}/\alpha$. We set the time scales to be the maximum length of time used in the electron microscopy images from You et al. [27], therefore $T = 24$ hr. For the length scales, we use the diameter of the cell from our simulations, making $L = 6$ μm.

3. Numerical Simulations

The model presented in Equations (12) is capable of simulating different types of topological transitions underlying the apoptotic phenomenon occurring in cells when induced by the presence of an apoptotic phase field. Here, we simulate specific characteristics of apoptotic processes, namely finger formation, fragmentation, and nucleation as seen in the work by You et al. [27], with the aim of understanding parameter values triggering different transitions.

3.1. **Physical and Numeric Parameter list.** Parameter values required to replicate the cellular dynamics shown throughout this manuscript are listed in Table 1. The dynamic moduli α and τ are chosen such that the dynamics of the phase field φ evolve more slowly than those of the phase field σ. This reflects the intracellular process in which the cell's response to the apoptotic agent occurs at a slower rate than the consumption of the agent itself.

Table 1. Physical and chemical parameters required for simulating apoptosis. The parameters ℓ_σ^2, ℓ_φ, ℓ_r^φ, ℓ_r^σ and k_2 are explored, and example values have been proposed in this table with the corresponding simulation for illustration.

Parameter	Value	Physical description
ℓ_f	3.33×10^3	Defines the order of separation for φ
ℓ_φ	1.33×10^{-4}	Ratio of interface width and dynamic modulus
ℓ_r^φ	960 (Figure 3), 4240 (Figure 6)	Chemical reaction parameter for φ
ϑ	25	Degree of anisotropy
ℓ_1	1.0	Ratio for interface width and relaxation time for σ
ℓ_2	1.5 (Figure 2)	Ratio of annihilation and dynamic modulus for σ
ℓ_r^σ	0.28 (Figure 3), 1.27 (Figure 6)	Chemical reaction parameter for σ
k_2	8.0 (Figure 3), 1.0 (Figure 6)	Parameter required for recreating reaction dynamics
ς_φ^p	0	Stoichiometric coefficient for the production of φ
ς_φ^r	1	Stoichiometric coefficient for the reactant required for φ
ς_σ^r	1	Stoichiometric coefficient for the reactant required for σ

In this piece of work, we want to observe the effect on the morphological transitions of the cell during apoptosis. Thus, we vary and explore the reaction rate parameters k_1 and k_2, and thus vary the dimensionless parameters ℓ_r^φ and ℓ_r^σ. Additionally, we will explore the parameter β, found in the dimensionless parameter ℓ_2. However, as $\dot{\varphi}$ decreases, this will act as a sink term for σ, thus increasing the amount of consumption.

The annihilation rate refers to the rate by which the cyto phase field is degraded by the apoptotic phase field. The rate of reaction is the rate at which the cell consumes the apoptotic phase field.

3.2. **Initial conditions.** All simulations were conducted on a 512×512 square grid using a Real Fourier basis and a fourth-order Runge–Kutta scheme for time integration. A dealiasing factor of 3/2 was applied to prevent aliasing errors. Preliminary convergence tests were performed to ensure mesh independence. The time step was fixed at $\Delta t = 1 \times 10^{-5}$, selected after analysing step sizes in the range $\Delta t \in [10^{-3}, 10^{-7}]$. This value was found to be sufficiently small to avoid spurious numerical artefacts. Similarly, simulations performed with resolutions of 128×128, 256×256, 512×512, and 1024×1024 demonstrated that the 512×512 grid provides an optimal balance between numerical accuracy and computational efficiency.

While cellular shape can vary depending on cell type and environment [28], we restricted the cyto and apoptotic phase fields to circular shapes, with the addition of noise to mimic cellular inhomogeneities. In what follows, we define the initial conditions and noise. The noise standard deviation is $a = \sqrt{0.1}$ and normally distributed as $\eta(x, y) \sim \mathcal{N}(0, a^2)$.

$$
\begin{cases}
S_0(\boldsymbol{x}) = \dfrac{1}{2}\left[1 - \tanh\left(\dfrac{(\boldsymbol{x} - \boldsymbol{x}_0)^2 - R_0^2}{\tilde{\epsilon}}\right)\right] + \eta, \\
S_1(\boldsymbol{x}) = \dfrac{1}{2}\left[1 - \tanh\left(\dfrac{(\boldsymbol{x} - \boldsymbol{x}_1)^2 - R_1^2}{\tilde{\epsilon}}\right)\right] + \eta, \\
\varphi(\boldsymbol{x}, 0) = \min\{1, \max\{0, S_0(\boldsymbol{x})\}\}, \\
\sigma(\boldsymbol{x}, 0) = \min\{1, \max\{0, S_1(\boldsymbol{x})\}\}, \\
\theta(\boldsymbol{x}, 0) = 0, \\
\epsilon(\theta_0) = \tilde{\epsilon}\left(1 + \vartheta \cos(\theta_0)\right), \\
\qquad \text{subject to periodic boundary conditions on } \partial\mathcal{D} \times (0,\ T).
\end{cases}
\tag{16}
$$

3.3. **Finger formation and nucleation during apoptosis.** In Equation (12), we describe the apoptotic degradation of the cyto phase field φ while the apoptotic phase field σ initiates the degradation. Figure 2 provides simulations illustrating the cyto phase field degradation when the interface is selected to be $\ell_\varphi = 1.33 \times 10^{-4}$ and the remaining parameters are $\ell_\sigma^2 = 1.5$, $\ell_r^\varphi = 960$, $\ell_r^\sigma = 0.28$ and $k_2 = 10.0$. This value of ϵ is chosen to produce a sharp interface based on the length scales for the size of the cyto phase field. In the simulation output, the cyto phase field σ diminishes at a high rate, producing the formation of distinct fingers, at the expense of the apoptotic phase field φ. It can also be seen that nucleations can form in the cyto phase field. Based on the proposed model for the type of reaction included in Equations (2), degradation of the phase field φ is promoted at the interface, that is, when $0 < \varphi < 1$. Therefore, inhomogeneities in the initial conditions allow for reactions to occur in the interior of the cyto phase field, hence enabling nucleations to form. However, these nucleations happen at a much lower rate. For this reason, it can be seen that the apoptotic phase field is consumed at the cyto phase field interface (membrane), starting at $\bar{t}$=3.98 and continuing in $\bar{t}$=7.99 and $\bar{t}$=11.76.

3.4. **Interface width influence.** The width of the interface between the phase fields is dictated by the dimensionless parameter ℓ_φ; thus, increasing ℓ_φ will increase the interface thickness and enlarge the area where the reaction is predominant.

It is known in phase field models that changes to the interface width can have a range of effects on the resulting dynamics, as a broader interface leads to a loss of detail in the simulation, as stated by Qin and Bhadeshia [24]. As can be seen in Figures 3, 4, and 5, a lower $\tilde{\epsilon}$ value sharpens the interface, while at larger values, the phase field has a diffuse interface. Figure 5 has a ratio of interface width to dynamic modulus of $\ell_\varphi = 2.133 \times 10^{-3}$, and here, there is no finger formation during the degradation and degradation of the phase field φ. However, by reducing $\ell_\varphi = 5.333 \times 10^{-4}$ (Figure 4), fingers begin to form during the degradation of the phase field φ. At $\ell_\varphi = 1.333 \times 10^{-4}$, finger formation in φ is more distinct compared to simulations obtained with higher values for ℓ_φ, as can be seen in Figures 4 and 5.

As seen in the bottom right-hand corner of Figure 4 (C) and in Figure 5 (B), (C), and (D), there is a pinch-off (fragmentation) from the finger during phase field φ degradation. This effect occurs at a specific interface width and cannot be found when $\ell_\varphi = 1.333 \times 10^{-4}$. The pinch-off results from the larger surface area present due to a larger interface width, hence promoting a higher number of reactions and faster

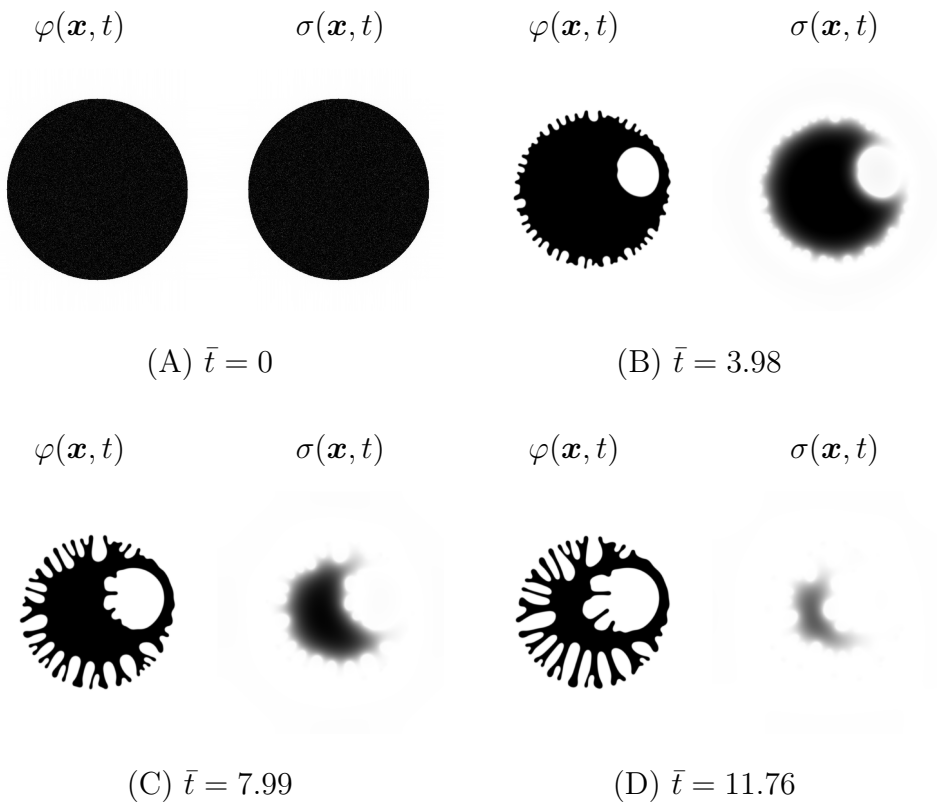

FIGURE 2. Progression of the φ and σ phase fields at the following nondimensionalised time points at $\bar{t} = 0.00$ (A), 3.98 (B), 7.99 (C), 11.76 (D). Using parameter values of: $\ell_\varphi = 1.333 \times 10^{-4}$, $\ell_2 = 1.5$, $\ell_r^\varphi = 960$, $\ell_r^\sigma = 0.28$ and $k_2 = 10.0$. The remaining parameters are listed in Table 1.

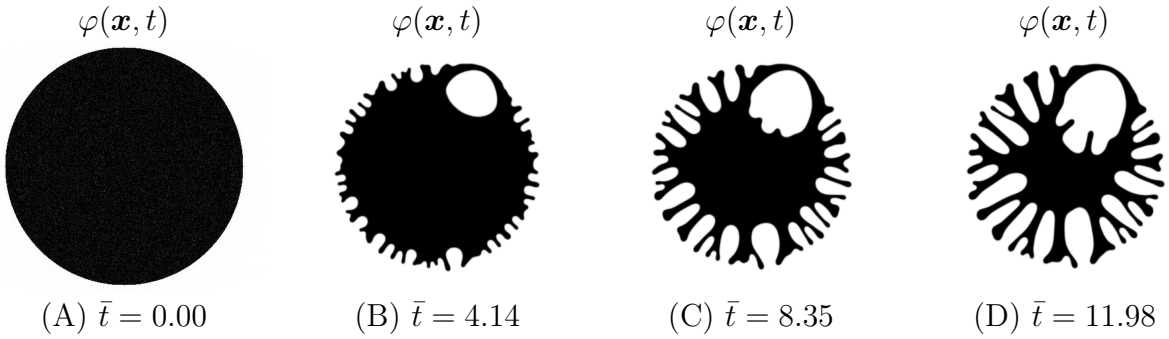

FIGURE 3. Evolution at nondimensionalised time $\bar{t} = 0.00$, (A) 4.14 (B), 8.35 (C), 11.98 (D) of the phase field φ with $\ell_\varphi = 1.333 \times 10^{-4}$, $\ell_2 = 1.5$, $\ell_r^\varphi = 960$, $\ell_r^\sigma = 0.28$, and $k_2 = 8.0$. The remaining parameters required to recreate the simulation are as listed in Table 1. Distinct finger formation can be observed.

topological transition of the phase field φ. Here, we analyse two sets of reaction rate parameters, given by $(k_1, k_2) \in \{(0.9, 10.0), (0.9, 8.0), (4.0, 1.0)\}$. The choice of these parameters influences the behaviour of $r(\varphi, \sigma)$ in Equation (13). When $k_1 = 4.0$ and $k_2 = 1.0$, the reaction term r approximates $r \approx g(\varphi)\sigma$. In contrast, the parameter choices $(k_1, k_2) = (0.9, 10.0)$ or $(0.9, 8.0)$ yield an approximation of $r \approx g(\varphi)\sigma^{1/3}$. However, implementing r directly in this latter form leads to numerical instabilities; therefore, the expression for r as presented in Equation (13) is preferred.

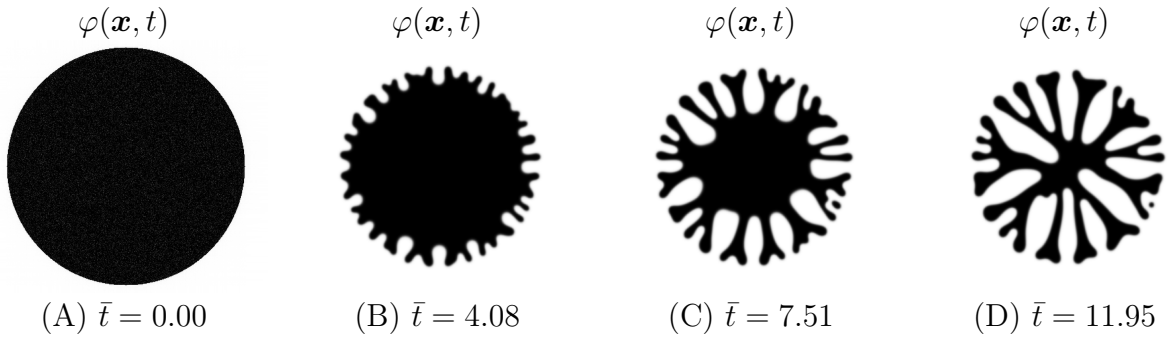

FIGURE 4. Evolution at $\bar{t} = 0$ (A), 4.08 (B), 7.51 (C), 11.95 (D) of φ with interface width increased to $\ell_\varphi = 5.333 \times 10^{-4}$, $\ell_2 = 1.5$, $\ell_r^\varphi = 960$, $\ell_r^\sigma = 0.28$ and $k_2 = 8.0$. The remaining parameters required to recreate the simulation are as listed in Table 1. Finger formation in $\varphi(\boldsymbol{x}, t)$ can be observed as forming during the degradation of the phase field. A fragment can be seen to form from one finger.

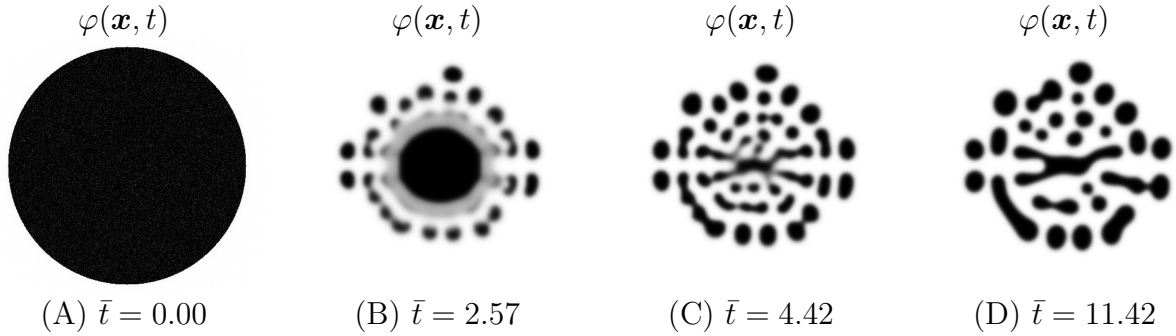

FIGURE 5. Evolution at nondimensionalised time $\bar{t} = 0.00$ (A), 2.57 (B), 4.42 (C), 11.42 (D) of φ with an interface width $\ell_\varphi = 2.133 \times 10^{-3}$, $\ell_2 = 1.5$, $\ell_r^\varphi = 960$, $\ell_r^\sigma = 0.28$, and $k_2 = 8.0$. The remaining parameters required to recreate the simulation are as listed in Table 1. No finger formation observed around the interface and fragmentation of the phase field $\varphi(\boldsymbol{x}, t)$ during apoptosis.

3.5. **Varying the rate of reaction and annihilation.** The parameters β, k_1, and k_2 are essential for controlling the rate at which the phase fields φ and σ degrade and are consumed, respectively. Varying these parameters allows for a wide range of dynamics and, therefore, a wide range of dynamic and steady state behaviour may be observed. In this section, the interface width is kept as $\ell_\varphi = 1.33 \times 10^{-4}$ to evaluate the effect of the other parameters.

3.5.1. *Rate of apoptosis when varying the rate of reaction parameters.* Varying k_1 or k_2 can greatly affect the rate of degradation exhibited by the cyto phase field φ; thus, exhibiting different dynamics in terms of nucleation and fragmentation.

Figure 6 shows a simulation with the same parameter choice for ℓ_φ and ℓ_2 as shown in Figure 3, with the changed parameter value for $k_1 = 4.0$ and $k_2 = 1.0$, hence promoting a faster reaction, therefore $\ell_r^\varphi = 4240$ and $\ell_r^\sigma = 1.27$. This can be seen by the evolution shown in Figure 6, where a rapid decline in the area covered by phase field φ occurs in comparison to the area covered by the phase field φ in Figure 3. Furthermore, the number of fragments during the simulation increases, indicating that a greater k_1 and k_2 produces a higher chance of fragmentation. Hence, the k_1 and k_2 parameters can be tuned to reflect the speed of enzymatic disassembly exerted by phase field σ, thus increasing the number of fragments. Furthermore, the values of $k_1 = 0.9$ and $k_2 = 10.0$ (see Figure 3) produce a different reaction profile to $k_1 = 4.0$ and $k_2 = 1.0$ (see Figure 6).

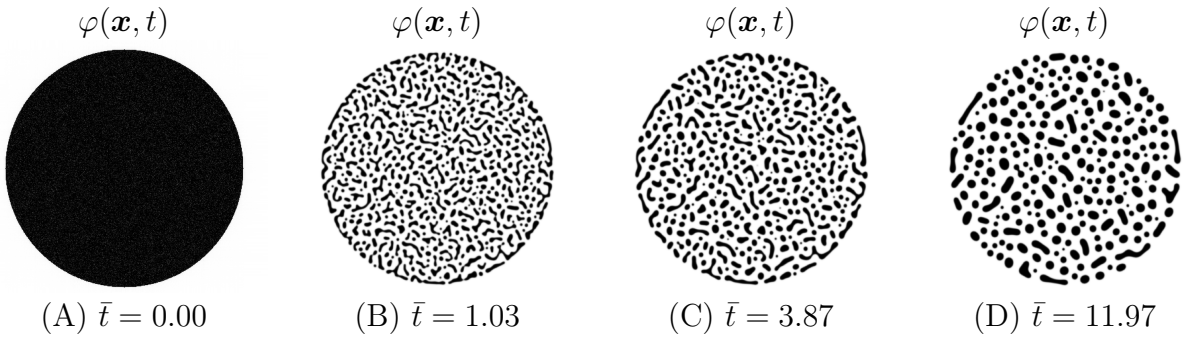

FIGURE 6. Evolution at $\bar{t} = 0.00$ (A), 1.03 (B), 3.87 (C), 11.97 (D) of the phase field φ with $\ell_\varphi = 1.333 \times 10^{-4}$, $\ell_2 = 1.5$, $\ell_r^\varphi = 4240$, $\ell_r^\sigma = 1.3$, and $k_2 = 1.0$. The remaining parameters have the values listed in Table 1. A higher reaction rate leads to the formation of a greater number of fragments when compared with Figure 3.

3.5.2. *Varying the rate of annihilation for the cell.* In the system shown in Equations (12), the rate of annihilation is described by β. This can be seen as the delay experienced when the phase field σ is consumed, and the phase field φ is degraded. Therefore, as β increases, it is expected that the conversion of the phase field σ into a reduction in the area of the phase field φ becomes less effective over time.

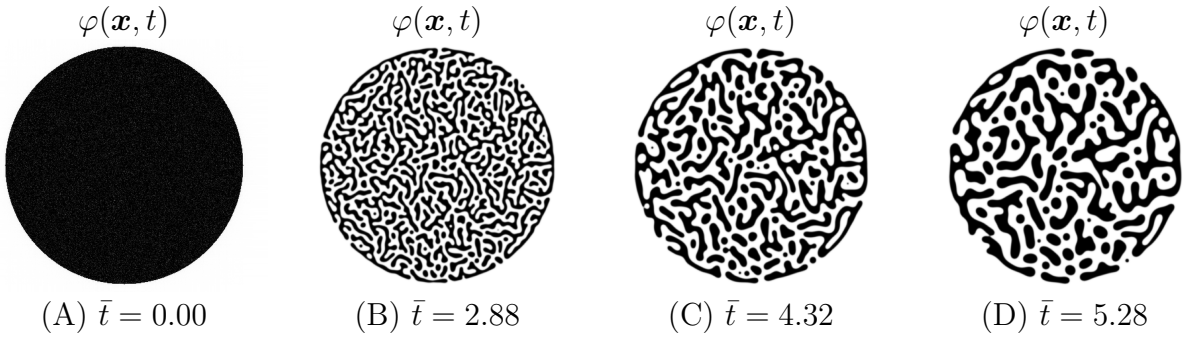

FIGURE 7. Evolution at $\bar{t} = 0.00$ (A), 2.88 (D), 4.32 (C), 5.28 (D) of the phase field φ with $\ell_\varphi = 1.333 \times 10^{-4}$, $\ell_2 = 2.0$, $\ell_r^\varphi = 4240$, $\ell_r^\sigma = 1.3$, and $k_2 = 1.0$. The remaining parameters are listed in Table 1. Larger fragments form when $\beta = 1.5$ and no nucleation.

Figure 7 shows an apoptotic simulation where $\ell_2 = 2.0$, $k_1 = 4.0$ ($\ell_r^\varphi = 4240$ and $\ell_r^\sigma = 1.27$), $k_2 = 1.0$ and $\ell_\varphi = 1.33 \times 10^{-4}$. When comparing to Figure 6, the degree of fragmentation is less advanced, thus demonstrating that lower ℓ_2 values result in larger fragmentation.

Comparing Figure 8 ($\ell_2 = 5.0$) with Figure 6 ($\ell_2 = 1.5$), we see that the use of $\ell_2 = 5.0$ results in an increased number of nucleation sites and no fragmentation taking place. Furthermore, when compared to Figure 3 ($\ell_2 = 1.5$, $\ell_r^\varphi = 960$, $\ell_r^\sigma = 1.27$ and $k_2 = 10.0$) nucleation can be seen in both simulations. However, finger formation is only present in Figure 3, and fragmentation is not present in either simulation. For $\ell_2 = 2.0$ (Figure 7), we observe that both nucleations and fragmentations are present. At the time point of $\bar{t} = 2.88$, the number of fragments is greater, and the nucleations are not well defined. However, as phase separation progresses and at $\bar{t} = 5.28$, large, well-defined nucleation sites are observed. Indicating that nucleations and fragments can coexist and fragments can transition into nucleations through phase separation.

3.6. **Internal configurational forces.** Here, we compute the internal configurational force, given in Equation (22) in Appendix A, to analyse the driving forces triggering the different topological transitions described in previous sections. We restrict attention to regions surrounding the cyto phase field and nucleations, as depicted in Figure 2.

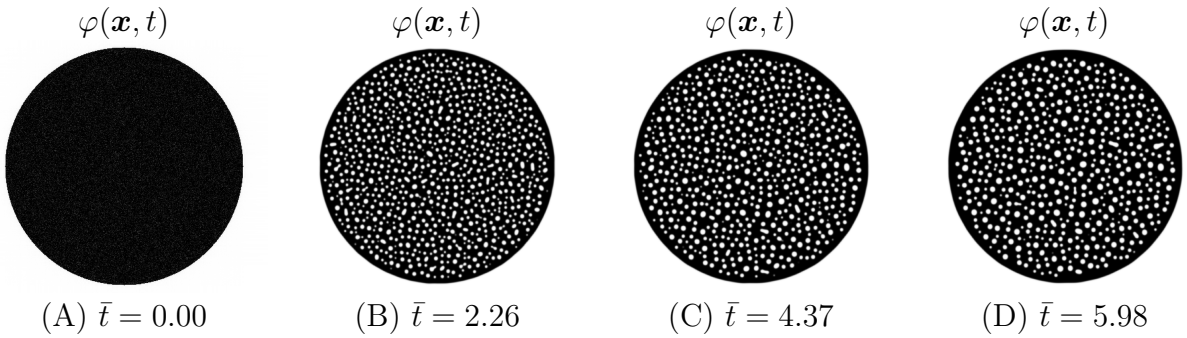

FIGURE 8. Evolution at $\bar{t} = 0.00$ (A), 2.26 (B), 4.37 (C), 5.98 (D) of the phase field φ with $\ell_\varphi = 1.333 \times 10^{-4}$, $\ell_2 = 5.0$, $\ell_r^\varphi = 4240$, $\ell_r^\sigma = 1.3$, and $k_2 = 1.0$. The remaining parameters are listed in Table 1. Nucleation is increased, and fragmentation is decreased compared to $\beta = 1.5$ in Figure 6.

Figure 9 shows details of the interface encompassing the cyto phase field φ and the apoptotic phase field σ with arrows representing the internal configurational forces. At $\bar{t} = 0.19$, in Figure 9 (A), the internal configurational force $\boldsymbol{f}$ is nearly uniform in space along the interface. Therefore, the interfaces for the phase fields φ and σ degrade uniformly. As time progresses to $\bar{t} = 1.20$, Figure 9 (B), the internal configurational oscillates along the interface. Thus, it produces the early stages of finger formation. At $\bar{t} = 2.64$ and 3.84, Figures 9 (C) and (D), distinct fingers form in the phase field φ. Furthermore, the magnitude of the internal configurational forces increases at the basin of the opening that forms between two fingers.

Figure 10 depicts the development of internal configurational forces during nucleation as the phase fields φ and σ degrade. At $\bar{t} = 0.41$, Figure 10 (A), the internal configurational force has a greater magnitude at the nucleation interface than at the main interface surrounding the phase field φ. The same behaviour can be observed in the phase field σ. Even though the nucleation appears to be circular, in Figure 10 (A), the magnitude of the internal configurational force along the interface surrounding the nucleation is not uniform. Despite the disuniformity in the internal configurational force magnitude, the cavity expands rapidly in all directions. As the simulation progresses to $\bar{t}$=1.44 (Figure 10 (B)), 2.64 (Figure 10 (C)), and 3.84 (Figure 10 (D)), the internal configuration force disappears at the nucleation interface closest to the interface encompassing the bulk of phase fields φ and σ. Therefore, the reduction in the degradation of the phase field φ results from the phase field σ no longer being present in the space between the nucleation and the main interface. At the later time points$\bar{t}$=1.44 (Figure 10 (B)), 2.64 (Figure 10 (C)), and 3.84 (Figure 10 (D)), the apoptotic phase field σ has reacted with the cyto phase field φ and been completely depleted. After the apoptotic phase field is consumed, the internal configurational force vanishes, and the degradation in the cyto phase field φ ceases. In the lower area of the nucleation at $\bar{t} = 3.84$ (Figure 10 (D)), it is observed that the magnitude of the internal configurational forces develops in two distinct regions on either side of a finger forming.

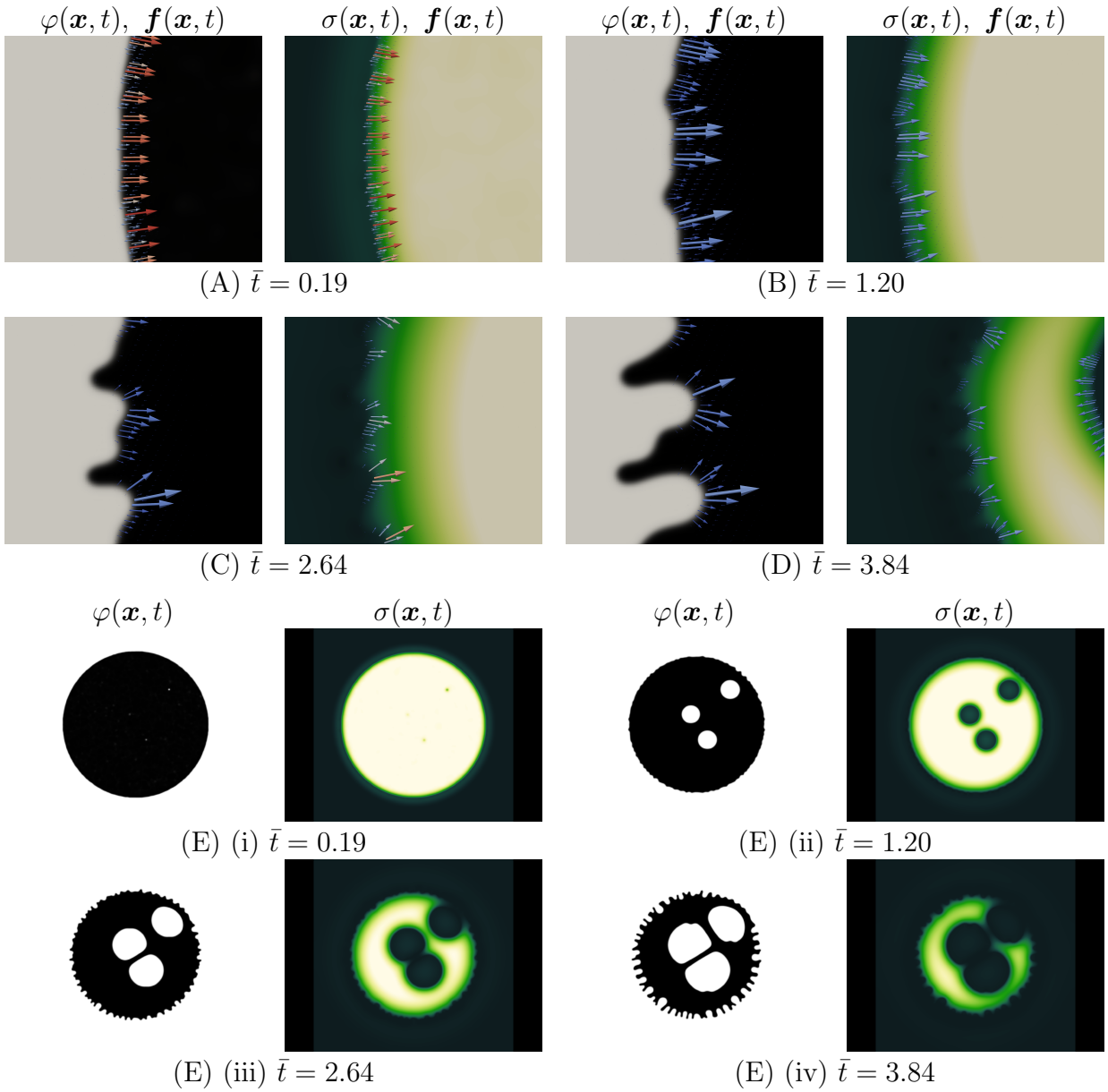

FIGURE 9. Evolution of a section of the interface for the phase fields φ and σ, and the internal configurational forces $\boldsymbol{f}$, and $|\boldsymbol{f}|$ at $\bar{t}$=0.19 (A, E(i)), 1.20 (B, E(ii)), 2.64 (C, E(iii)), and 3.84 (D, E(iv)). The parameters selected for this simulation as listed in Table 1, $\ell_\varphi = 1.333 \times 10^{-4}$, $\ell_2 = 1.5$, $\ell_r^\varphi = 960$, $\ell_r^\sigma = 0.28$, and $k_2 = 8.0$. The arrows in images (A), (B), (C), and (D) indicate the direction of $\boldsymbol{f}$; their size reflects the relative magnitude, while the colour represents the magnitude throughout the simulation—red denotes higher values than blue. In E(i-iv), the $|\boldsymbol{f}|$ is overlayed with the phase-field $\varphi(\boldsymbol{x},t)$ with red regions indicating a greater magnitude and blue regions indicating a lower magnitude.

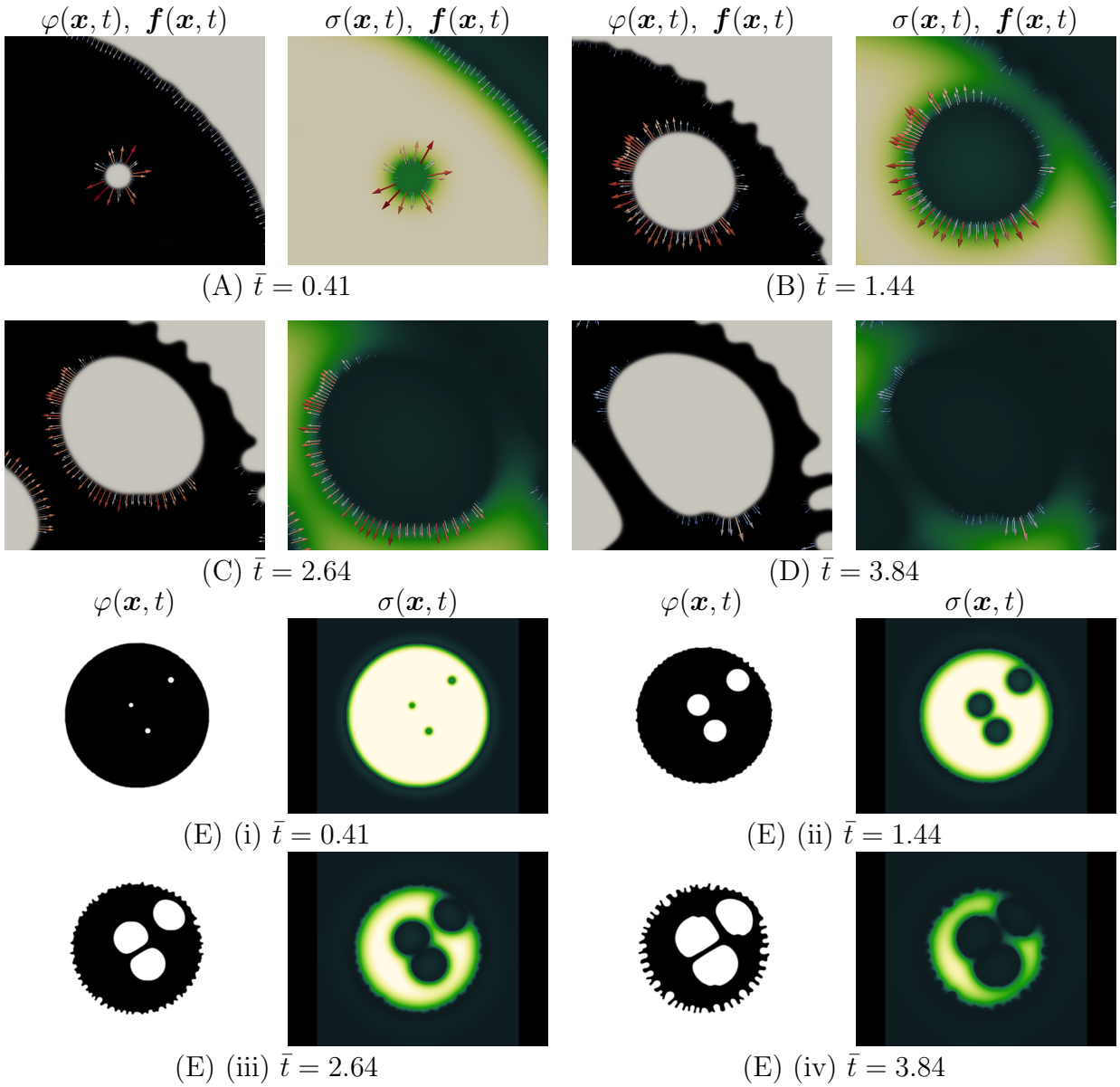

FIGURE 10. Evolution of a nucleation in φ and σ. The internal configurational force $\boldsymbol{f}$ is present at the nucleation interface. The nucleation is at $\bar{t}$=0.41 (A, E(i)), 1.44 (B, E(ii)), 2.64 (C, E(iii)), and 3.84 (D, E(iv)).The parameters selected for this simulation as listed in Table 1, $\ell_\varphi = 1.333\times10^{-4}$, $\ell_2 = 1.5$, $\ell_r^\varphi = 960$, $\ell_r^\sigma = 0.28$, and $k_2 = 8.0$. The arrows in images (A), (B), (C), and (D) indicate the direction of $\boldsymbol{f}$; their size reflects the relative magnitude, while the colour represents the magnitude throughout the simulation—red denotes higher values than blue. In E(i-iv), the $|\boldsymbol{f}|$ is overlayed with the phase-field $\varphi(\boldsymbol{x},t)$ with red regions indicating a greater magnitude and blue regions indicating a lower magnitude.

4. Qualitative comparison of electron microscopy images and simulations

For a qualitative comparison between our apoptotic simulations and electron microscopy images, we used binarised images from You et al. [27]. These show prostate cancer cells exposed to an anti-cancer drug, KML001, which is known to induce apoptosis. We compared and identified similar structures and topological transitions between the electron microscopy and the simulation images to demonstrate the model's capabilities. The cyto phase field φ in our model setup was compared to electron microscopy images of prostate cancer cell lines PC3, DU145, and LNCaP [27] to determine whether similar morphological changes were taking place in both systems. In this comparison, KML001 was approximated to act as the apoptotic phase field σ; however, this phase field cannot be visually compared to KML001, so we focused on the comparison between the cyto phase field φ and cell images.

As mentioned previously, the predominant focus of our model was placed on simulating key apoptotic features: finger formation, cell shrinkage, fragmentation and nucleation. In our simulations, the cyto phase field φ exhibits all characteristics. Starting with finger formation, we provide a binarised version of an electron microscopy image exhibiting this feature from [27]. To supplement the electron microscopy image demonstrating this characteristic, we include a simulation from our model that provides similar features in Figure 11. As can be seen from the comparisons, finger formation is present in both the microscopy image of a PC3 cell (A) and the simulation (B), as well as the nucleation. Thus, thermodynamic processes described by our model also occur when the cancerous cell is exposed to the anti-cancer drug. (A) differs from (B) in the aspect of fragmentation, with more pronounced cell fragments around the prostate cancer cell present in the microscopy image. However, it can be seen in Figure 4 that fragments of the cyto phase field φ can form during the degradation of the phase field as a result of apoptosis. In this simulation, the fragmentation appeared as the parameter dictating the interface width $\tilde{\epsilon}$ and thus the dimensionless parameter ℓ_φ was increased. Fragmentation of the phase field φ was also observed when the reaction rate parameters k_1 was increased and k_2 was decreased, see Figures 6 and 7. Thus, depending on the experimental conditions, different cellular morphologies can be observed, hence explaining the variation in the comparisons.

Another key characteristic of apoptosis observed in the electron microscopy images in [27] is the nucleation, that is, the formation of cavities. Figure 11 exhibits the nucleation in the electron microscopy image (A) and the simulation (B). However, a more pronounced representation of nucleation can be seen in Figure 12, where two large cavities can be seen at the interface in both the microscopy image of a PC3 cell (A) and the simulation (B). In both images, it is observed that the structure surrounding the nucleation is maintained over a greater time course than the integrity of the primary region of the cyto phase field φ. This could be explained in our simulations by the nonexistence of the apoptotic phase field σ. Thus, further degeneration of the cyto phase field φ surrounding the nucleation could not occur, and the structure around the nucleation persists. Furthermore, it was observed in Figure 9 that the internal configurational force at the interface vanishes around the nucleation and only exists where the phase field σ is still present.

In the electron microscopy images presented by You et al. [27], the LNCaP cell line noticeably forms a greater number of cavities in the cell, and the cavities appear in higher frequency compared to those in PC3 cells. This can be seen in Figure 13 and is compared to the results from our simulation seen in Figure 8. Thus, we demonstrate we can account for these morphological changes in our simulations by introducing a higher rate of reaction for the degradation of the cyto phase field φ.

Although we aimed at the simplest theoretical model and, thus, we do not account for biological cells' chemical complexity and heterogeneity, our simulations are in good agreement with experimental data. It should be further noted that the different cell lines analysed by You et al. [27] exhibited different levels of sensitivity to the apoptotic phase field. This led to the administration of a 10 μM KML001 solution for PC3 cells and a 1 μM KML001 solution for LNCaP cells, which might cause the differences in morphological appearance observed. Nonetheless, the similarities between the model output and microscopy data demonstrate that we have developed a robust platform to model morphology changes in cells undergoing apoptosis physically. Interestingly, this further indicates that changes in cell morphology are thermodynamic responses over the course of apoptosis.

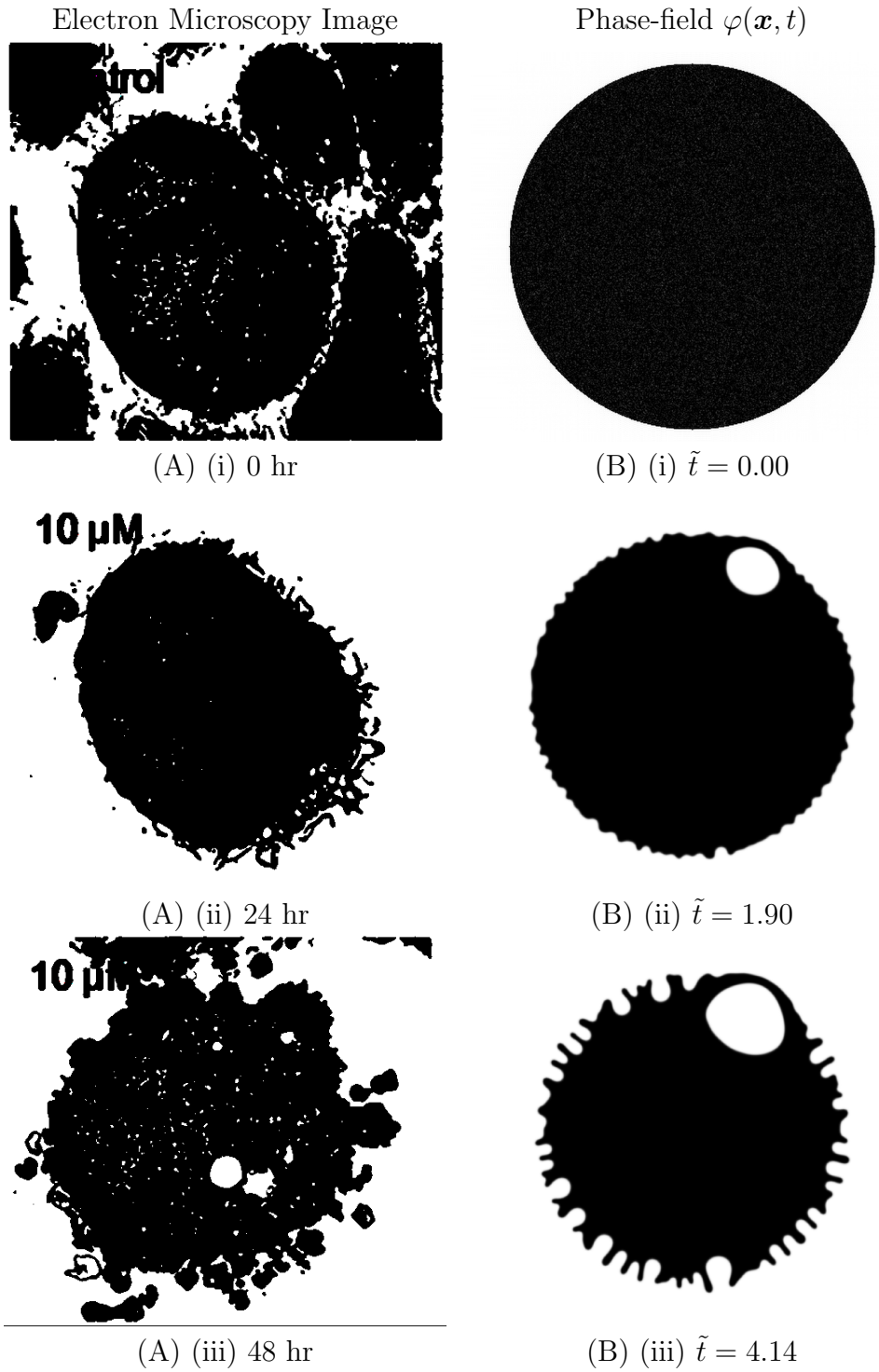

FIGURE 11. (A) (i-iii) Electron microscopy images by You et al. [27] of a PC3 prostate cancer cell undergoing apoptosis over 48 hours with 10 μM of KML001 added; (B) (i-iii) Time evolution of the phase field φ undergoing apoptosis induced by the phase field σ illustrating finger formation.

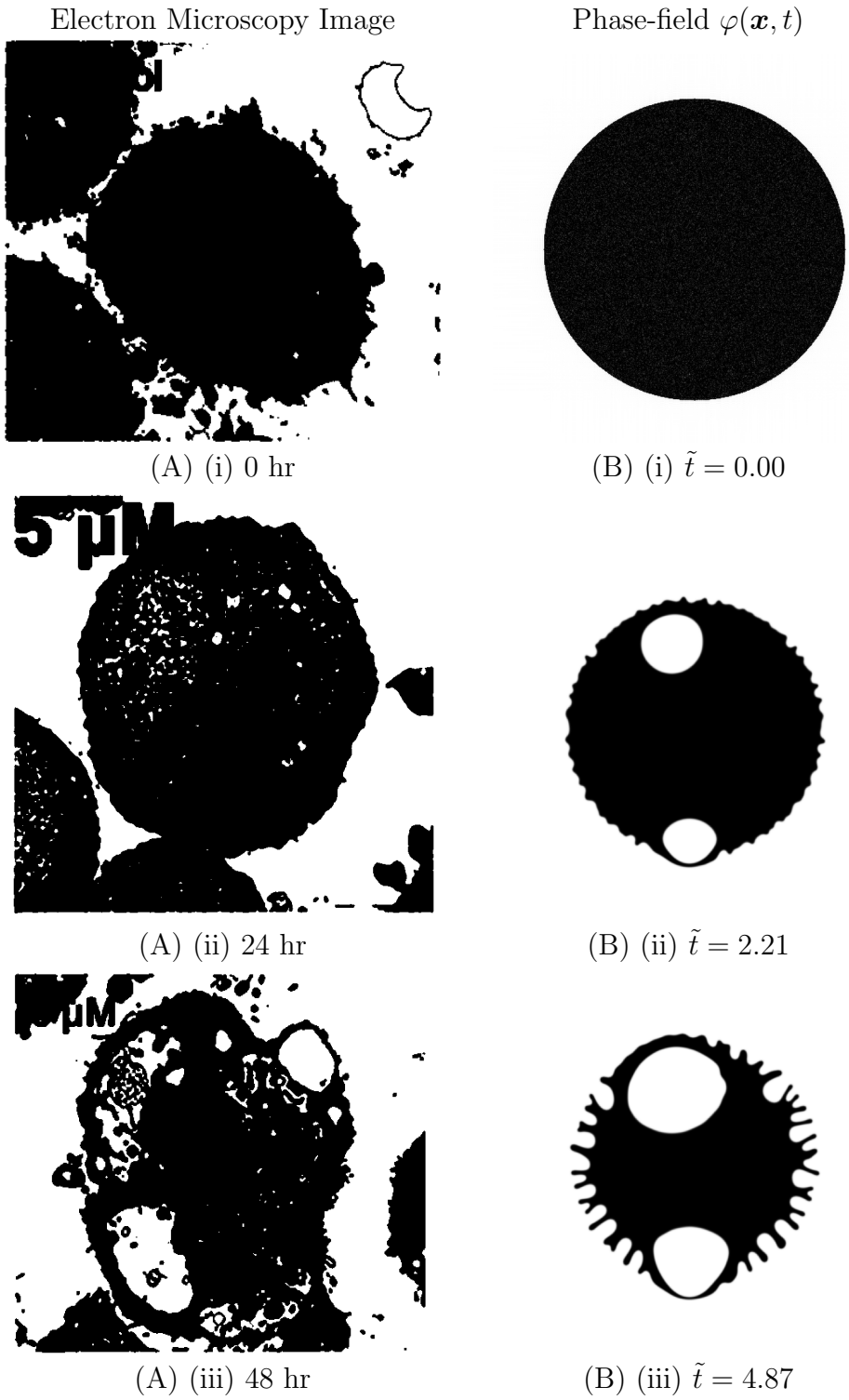

FIGURE 12. (A) (i-iii) Electron microscopy images by You et al. [27] of a DU145 prostate cancer cell line undergoing apoptosis over 48 hours with 10 μM of KML001 added; (B) Time evolution of the phase field φ undergoing apoptosis induced by the phase field σ illustrating nucleation and finger formation. This simulation utilised different noise in the initial condition than the images present in Figure 3.

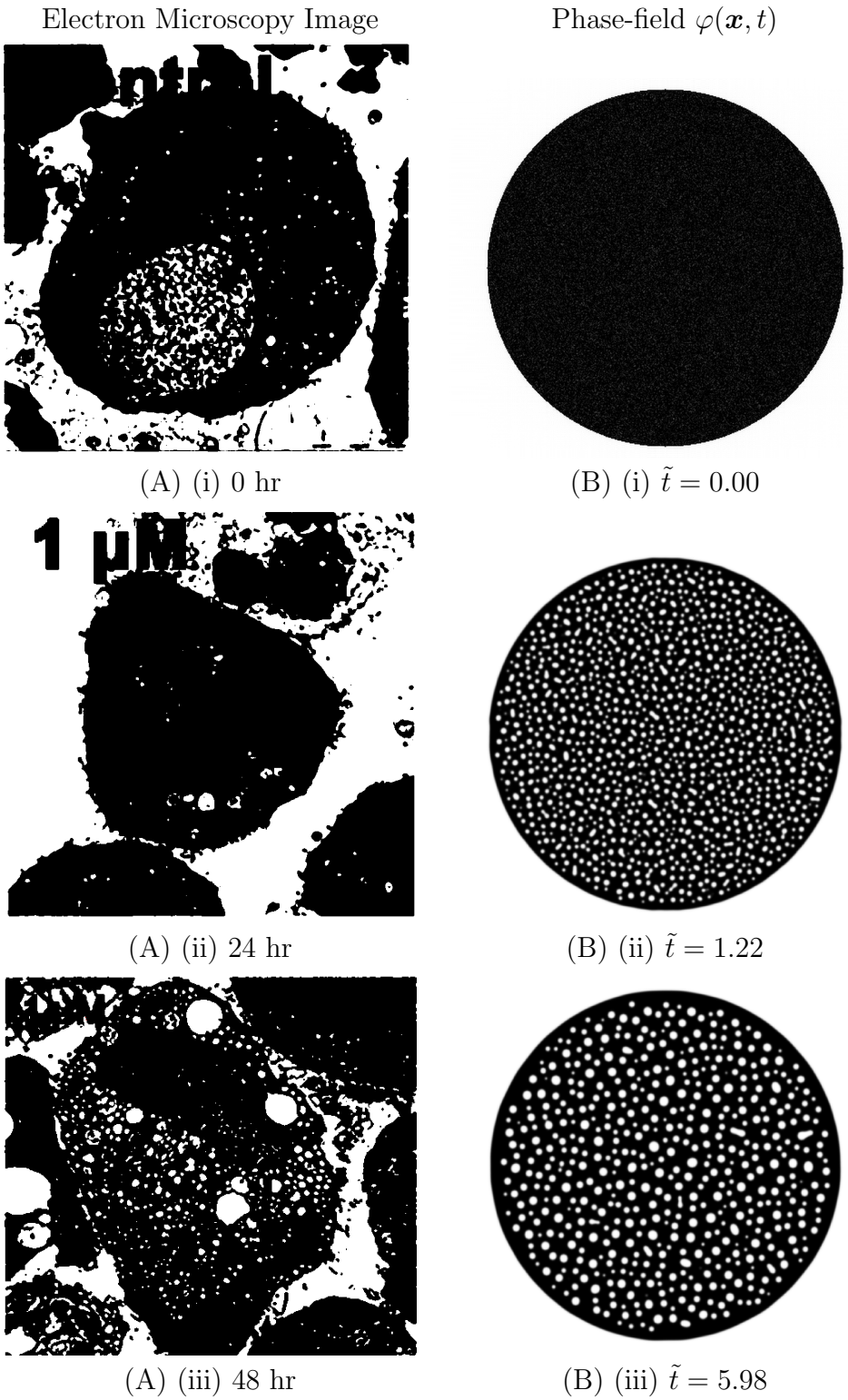

FIGURE 13. (A) (i-iii) Electron microscopy images by You et al. [27] illustrating nucleation in a greater number of the cell type LNCaP exposed to 1 μM KML001 at the 48 hr time point. (B) (i-iii) Simulation of the phase field $\varphi(\boldsymbol{x}, t)$ illustrating nucleation in a greater number with a higher rate of reaction k. See Figure 8 for the time evolution of the phase field and parameter choice to obtain the dynamics.

5. Conclusions

Apoptosis proceeds through two well-established signalling routes, that is, the intrinsic, mitochondria-mediated pathway and the extrinsic, receptor-mediated pathway, as discussed by Lossi [20] and Mustafa et al. [22]. Both mechanisms ultimately result in the activation of caspases, which coordinate the enzymatic disassembly of the cytoskeleton, organelles, and nucleus. In our formulation, this biochemical activation is represented by a spatially distributed apoptotic phase, coupled to a cyto phase describing the cell itself. The model treats the activation field in a pathway-agnostic manner, focusing on its mechanical and morphological consequences rather than its molecular origin.

We developed a biochemo–mechanical phase-field framework, given by the system in Equations (12), and implemented it in the Dedalus package [4]. Variational derivation yielded a coupled set of reaction–diffusion and configurational-mechanics equations capable of reproducing characteristic apoptotic morphologies and topological transitions. Simulations of the cyto phase φ interacting with the apoptotic phase σ reveal finger formation, nucleation, fragmentation, and shrinkage. The parameters ℓ_φ, ℓ_r^φ, ℓ_r^σ, k_2, and ℓ_2 control the onset and extent of these topological transitions: decreasing $\tilde{\epsilon}$ suppresses fragmentation, while larger ℓ_r^φ, ℓ_r^σ, k_2, and ℓ_2 enhance cavity and finger formation. Internal configurational-force analysis identifies zones of highest degradation, matching the protrusive regions observed experimentally.

Comparison with electron microscopy images from You et al. [27], where KML001 induces apoptosis and autophagic cell death in prostate cancer cells via oxidative stress, shows morphological agreement to a great extent. The model captures the same qualitative sequence of surface deformation, cavity formation, and eventual fragmentation observed in PC3 and LNCaP cells, confirming its ability to reproduce experimentally reported apoptotic morphologies. The discrepancies seen between the experimental and simulated data are due to the highly heterogeneous nature of the cytoplasm and the cell as a whole. Furthermore, the simulation utilises a simple initial condition where the cell is assumed to be a circular disk, in reality, cells appear in a myriad of shapes and sizes.

The Dedalus implementation establishes a foundation for future three-dimensional simulations, where further calibration against quantitative biological data could refine model parameters and enable predictive studies of cellular disassembly processes beyond the resolution of current microscopy techniques.

6. Acknowledgments

The Engineering and Physical Sciences Research Council (EPSRC) supported the project's funding via the Centre of Doctoral Training (CDT) in Transformative Pharmaceutical Technologies [EP/S023054/1]. We are grateful for access to the University of Nottingham's Ada HPC service. [LE] This work was partially supported by the Flexible Interdisciplinary Research Collaboration Fund at the University of Nottingham, Project ID 7466664.

7. Data Availability

The necessary code for simulation presented in this document can be found on the following https://github.com/Nonlinear-Phenomena-Lab/Phase-field-Apoptosis repository.

Appendix A. Configurational mechanics

The evolution of the interfaces may be described by configurational mechanics. This approach, proposed by Gurtin [15] generalises the concept of Newtonian forces. Configurational forces are connected to the integrity of the material in a broad sense, explaining the evolution of material and immaterial interfaces. In what follows, we use the configurational balance suggested by Fried [12] and Espath & Calo [11].

The underlying local configurational force balances may be stated as

$$\operatorname{div} \boldsymbol{C} + \boldsymbol{f} = \boldsymbol{0}, \tag{17}$$

where $\boldsymbol{C}$ is the configurational stress tensor and $\boldsymbol{f}$ is the internal configurational forces.

To determine the quantities entering the configurational balances, departing from the field Equations (9), we multiply the evolution of the phase field φ by $\nabla\varphi$ and the evolution of the phase field σ by $\nabla\sigma$, yielding

$$\begin{cases} (\tau\dot{\varphi} - (\varsigma_\varphi^p - \varsigma_\varphi^r)r)\nabla\varphi = -\left(\nabla\varphi\dfrac{\partial\psi}{\partial\varphi} - \operatorname{div}\left(\nabla\varphi\otimes\dfrac{\partial\psi}{\partial\nabla\varphi}\right) + \Delta\varphi\dfrac{\partial\psi}{\partial\nabla\varphi}\right), \\ (\alpha\dot{\sigma} - \beta\dot{\varphi} + \varsigma_\sigma^r r)\nabla\sigma = -\left(\nabla\sigma\dfrac{\partial\psi}{\partial\sigma} - \operatorname{div}\left(\nabla\sigma\otimes\dfrac{\partial\psi}{\partial\nabla\sigma}\right) + \Delta\sigma\dfrac{\partial\psi}{\partial\nabla\sigma}\right). \end{cases} \tag{18}$$

With the identity

$$\begin{aligned} \nabla\psi &= \frac{\partial\psi}{\partial\varphi}\nabla\varphi + \frac{\partial\psi}{\partial\sigma}\nabla\sigma + \frac{\partial\psi}{\partial\nabla\varphi}\Delta\varphi + \frac{\partial\psi}{\partial\nabla\sigma}\Delta\sigma, \\ &= \operatorname{div}(\psi\mathbf{1}), \end{aligned} \tag{19}$$

summing Equations (18) lead us to

$$(\tau\dot{\varphi} - (\varsigma_\varphi^p - \varsigma_\varphi^r)r)\nabla\varphi + (\alpha\dot{\sigma} - \beta\dot{\varphi} + \varsigma_\sigma^r r)\nabla\sigma = -\left(\operatorname{div}(\psi\mathbf{1}) - \operatorname{div}\left(\nabla\varphi\otimes\frac{\partial\psi}{\partial\nabla\varphi}\right) - \operatorname{div}\left(\nabla\sigma\otimes\frac{\partial\psi}{\partial\nabla\sigma}\right)\right). \tag{20}$$

The local configurational force balance resulting from Equation (17), gives the following configurational stress tensor

$$\boldsymbol{C} = \psi\mathbf{1} - \nabla\varphi\otimes\frac{\partial\psi}{\partial\nabla\varphi} - \nabla\sigma\otimes\frac{\partial\psi}{\partial\nabla\sigma}, \tag{21}$$

and the internal configurational force becomes

$$\boldsymbol{f} = (\tau\dot{\varphi} - (\varsigma_\varphi^p - \varsigma_\varphi^r)r)\nabla\varphi + (\alpha\dot{\sigma} - \beta\dot{\varphi} + \varsigma_\sigma^r r)\nabla\sigma. \tag{22}$$

References

[1] B. Alberts, A. Johnson, J. Lewis, M. Raff, K. Roberts, and P. Walter. Programmed cell death (apoptosis). In *Molecular Biology of the Cell. 4th edition*. Garland Science, 2002.

[2] Y. Bai, J. R. Mianroodi, Y. Ma, A. K. da Silva, B. Svendsen, and D. Raabe. Chemo-mechanical phase-field modeling of iron oxide reduction with hydrogen. *Acta Materialia*, 231:117899, 2022.

[3] D. Bertheloot, E. Latz, and B. S. Franklin. Necroptosis, pyroptosis and apoptosis: an intricate game of cell death. *Cellular & molecular immunology*, 18(5):1106–1121, 2021.

[4] K. J. Burns, G. M. Vasil, J. S. Oishi, D. Lecoanet, and B. P. Brown. Dedalus: A flexible framework for numerical simulations with spectral methods. *Physical Review Research*, 2(2):023068, 2020.

[5] C. Castillo Ferrer, K. Berthenet, and G. Ichim. Apoptosis–fueling the oncogenic fire. *The FEBS journal*, 288(15):4445–4463, 2021.

[6] S. Clavijo, L. Espath, and V. Calo. Extended Larché–Cahn framework for reactive Cahn–Hilliard multicomponent systems. *Continuum Mechanics and Thermodynamics*, 33:2391–2410, 2021.

[7] S. P. Clavijo, L. Espath, and V. M. Calo. Extended larché–cahn framework for reactive cahn–hilliard multicomponent systems. *Continuum Mechanics and Thermodynamics*, 33:2391–2410, 2021.

[8] S. P. Clavijo, L. Espath, A. Sarmiento, and V. M. Calo. A continuum theory for mineral solid solutions undergoing chemo-mechanical processes. *Continuum Mechanics and Thermodynamics*, 34:17–38, 2022.

[9] P. Colli, G. Gilardi, E. Rocca, and J. Sprekels. Optimal distributed control of a diffuse interface model of tumor growth. *Nonlinearity*, 30(6):2518, 2017.

[10] S. Elmore. Apoptosis: a review of programmed cell death. *Toxicologic pathology*, 35(4):495–516, 2007.

[11] L. Espath and V. Calo. Phase-field gradient theory. *Zeitschrift für angewandte Mathematik und Physik*, 72(2):45, 2021.

[12] E. Fried. On the relationship between supplemental balances in two theories for pure interface motion. *SIAM Journal on Applied Mathematics*, 66(4):1130–1149, 2006.

[13] E. Fried and M. E. Gurtin. Continuum theory of thermally induced phase transitions based on an order parameter. *Physica D: Nonlinear Phenomena*, 68(3-4):326–343, 1993.

[14] P. Gaziano and M. Marino. A phase-field model of cell motility in biodegradable hydrogel scaffolds for tissue engineering applications. *Computational Mechanics*, 74(1):45–66, 2024.

[15] M. E. Gurtin. *Configurational forces as basic concepts of continuum physics*, volume 137. Springer Science & Business Media, 1999.

[16] A. Hawkins-Daarud, K. G. van der Zee, and J. Tinsley Oden. Numerical simulation of a thermodynamically consistent four-species tumor growth model. *International journal for numerical methods in biomedical engineering*, 28(1):3–24, 2012.

[17] S. Kari, K. Subramanian, I. A. Altomonte, A. Murugesan, O. Yli-Harja, and M. Kandhavelu. Programmed cell death detection methods: a systematic review and a categorical comparison. *Apoptosis*, 27(7):482–508, 2022.

[18] R. Kobayashi. Modeling and numerical simulations of dendritic crystal growth. *Physica D: Nonlinear Phenomena*, 63 (3-4):410–423, 1993.

[19] F. J. Krambeck. The mathematical structure of chemical kinetics in homogeneous single-phase systems. *Archive for Rational Mechanics and Analysis*, 38(5):317–347, 1970.

[20] L. Lossi. The concept of intrinsic versus extrinsic apoptosis. *Biochemical Journal*, 479(3):357–384, 2022. doi: 10.1042/BCJ20210854.

[21] A. Moure and H. Gomez. Three-dimensional simulation of obstacle-mediated chemotaxis. *Biomechanics and modeling in mechanobiology*, 17(5):1243–1268, 2018.

[22] M. Mustafa and et al. Apoptosis: A comprehensive overview of signaling pathways, morphological changes and physiological significance and therapeutic implications. *Cells*, 13(22):1838, 2024. doi: 10.3390/cells13221838. URL `https://www.ncbi.nlm.nih.gov/pmc/articles/PMC11592877/`.

[23] C. Nössing and K. M. Ryan. 50 years on and still very much alive:'apoptosis: a basic biological phenomenon with wide-ranging implications in tissue kinetics'. *British journal of cancer*, 128(3):426–431, 2023.

[24] R. Qin and H. Bhadeshia. Phase field method. *Materials science and technology*, 26(7):803–811, 2010.

[25] I. Vitale, F. Pietrocola, E. Guilbaud, S. A. Aaronson, J. M. Abrams, D. Adam, M. Agostini, P. Agostinis, E. S. Alnemri, L. Altucci, et al. Apoptotic cell death in disease—current understanding of the nccd 2023. *Cell Death & Differentiation*, 30(5):1097–1154, 2023.

[26] S. M. Wise, J. S. Lowengrub, H. B. Frieboes, and V. Cristini. Three-dimensional multispecies nonlinear tumor growth—i: model and numerical method. *Journal of theoretical biology*, 253(3):524–543, 2008.

[27] D. You, Y. Kim, M. J. Jang, C. Lee, I. G. Jeong, Y. M. Cho, J. J. Hwang, J. H. Hong, H. Ahn, and C.-S. Kim. Kml001 induces apoptosis and autophagic cell death in prostate cancer cells via oxidative stress pathway. *PLoS One*, 10(9): e0137589, 2015.

[28] H. Zeng. What is a cell type and how to define it? *Cell*, 185(15):2739–2755, 2022.